Available online at www.sciencedirect.com

ScienceDirect

Advances in Space Research 77 (2026) 7240–7256

ADVANCES IN SPACE RESEARCH (a COSPAR publication)

www.elsevier.com/locate/asr

Ionospheric reconstruction from LEO-GNSS, LEO-PNT, and ground-GNSS using an information-filter

Lucas Schreiter [a,b,c,*], Andreas Brack [b], Benjamin Männel [b], Harald Schuh [a]

[a] Technical University of Berlin, Straße des 17. Juni 135, Berlin 10623, Germany
[b] GFZ Helmholtz Centre for Geosciences, Telegrafenberg, Potsdam 14473, Germany
[c] Deutsches Geodätisches Forschungsinstitut der Technischen Universität München, Arcisstraße 21, Munich 80333, Germany

Received 1 July 2025; received in revised form 5 December 2025; accepted 23 January 2026
Available online 30 January 2026

Abstract

This paper presents a theoretical study on ionospheric reconstruction using GNSS data obtained from Low Earth Orbit (LEO) satellites in a PNT (Position, Navigation, and Timing) configuration, where the LEO satellites not only receive but also transmit GNSS signals, which can be tracked by ground or mobile receivers. The study is intended to pave the way for incorporating slant Total Electron Content (TEC) data from ESA's upcoming LEO-PNT into ionospheric reconstructions. We generate synthetic slant TEC for three observation scenarios: Ground-GNSS, ground-LEO, and LEO-GNSS links. As ground-truth, the IRI-20 model with the Ozhogin plasmasphere extension is used. An inversion to recover the electron density from slant TEC observations is performed using an Extended Kalman Filter (EKF) in the information-filter formulation for all possible combinations of observation scenarios. As the LEO constellation, we will utilize existing LEO satellites that were available in May 2020, including Swarm, COSMIC-2, GRACE-FO, Jason-3, Sentinel-1, Sentinel-2, and Sentinel-3, as well as several Spire satellites. They cover a variety of altitudes between 400 km and 1350 km. For this study, we assume they could transmit dual-frequency GNSS-like signals like a PNT mission, which is not the case for any of the satellites mentioned. We only consider relative slant TEC to be insensitive to calibration biases that may reach a few TEC units. Given a real global ground-station network, LEO and GNSS satellites, we show that 15-min reconstruction solutions, only containing ground stations, cannot compete with solutions including LEO satellites. Furthermore, our results show that the joint use of LEO-POD (Precise Orbit Determination Antenna) and LEO-PNT (RMSE at 500 km: 0.95×10^{-4} cm^{-3}) provides superior performance compared to configurations where either is substituted by ground-based GNSS (ground-GNSS and PNT: 4.03×10^{-4} cm^{-3}; Gound-GNSS and POD 1.18×10^{-4} cm^{-3}). We also show that the reconstruction error roughly doubles when radio occultation measurements are omitted. The dependency of the error on the distribution of the ground stations is also shown. Areas with only a few or no ground stations show the lowest correlation between IRI-20 and the reconstructions, e.g., near Point Nemo, where the correlation drops to 0.5.

Keywords: Ionosphere reconstruction; LEO-PNT; Kalman-Filter

1. Introduction

The near-Earth environment hosts a complex, weakly ionized plasma, which is broadly divided into the ionosphere (up to roughly 1000 km) and the plasmasphere. The plasmasphere extends several Earth radii above this altitude (Kelley, 1989b; Bilitza, 1991; Vaishnav et al., 2021; Zhelavskaya et al., 2017). Both regions display pronounced spatio-temporal variability driven by solar wind dynamics, geomagnetic storms, and seasonal, diurnal, and nocturnal changes, with electron densities fluctuating by several orders of magnitude (Kelley, 1989a). Precise knowledge of the electron density along the signal path is

* Corresponding author.
E-mail address: lucas.schreiter@tum.de (L. Schreiter).

https://doi.org/10.1016/j.asr.2026.01.078

essential for single-frequency Global Navigation Satellite Systems (GNSS), as it can induce range errors of several meters (Klobuchar, 1987). Accurate real-time and near-real-time modeling and monitoring of electron density not only deepens our understanding of space weather effects but also enhances a wide range of technological applications.

Over the past decades, ground- and space-based techniques, including radars, ionosondes, in situ satellite instruments, and Total Electron Content (TEC) retrievals from GNSS, have enabled significant advances in ionospheric science (Bilitza et al., 2022). These measurements underpin empirical models such as the International Reference Ionosphere (IRI), now in its IRI-20 release (Bilitza et al., 2022), and assimilation-based frameworks like the Utah State University Global Assimilation of Ionospheric Measurements (USU-GAIM) model (Schunk et al., 2004). Additional approaches utilize satellite data directly, as in Hoque and Jakowski (2008); Gerzen and Minkwitz (2016), or leverage machine learning for estimating electron density or the key parameters of ionospheric profiles in the topside ionosphere and plasmasphere (Smirnov et al., 2023; Zhelavskaya et al., 2021).

The global distribution of GNSS ground stations makes GNSS a powerful tool for mapping ionospheric and plasmaspheric electron content. Free electrons cause code delays and carrier phase advances in GNSS signals, allowing estimation of integrated electron density along propagation paths (slant TEC or sTEC) (Fritsche et al., 2005). However, conventional TEC mapping typically compresses all electrons into a thin layer near 350—450 km altitude (Schaer et al., 1996). This simplification can introduce errors when analyzing Low Earth Orbit (LEO) satellite data, which samples only segments of the total TEC.

A comprehensive three-dimensional (3D) picture of the ionosphere requires augmenting ground-based GNSS networks with LEO satellites, whose diverse geometries enable improved vertical resolution and support tomographic reconstruction (e.g., Norberg et al. (2016)). Data assimilation and tomographic techniques, such as those applied to COSMIC TEC data via 3D variational assimilation (Nikoukar et al., 2015a) and voxel-based algebraic reconstruction (Prol et al., 2023), have demonstrated potential, including simulated inter-satellite links in LEO constellations. However, voxel-based methods, such as the Algebraic Reconstruction Technique (ART) and Multiplicative ART (MART), can suffer from poor observation geometry, especially in regions where ray coverage is sparse or uneven, leading to singularities and unreliable reconstructions Bust and Mitchell (2008). These limitations are pronounced in global ionospheric tomography, where the distribution of satellite-ground links may leave large regions underconstrained.

LEO-PNT (Position, Navigation, and Timing) satellites, as they promise a wide variety of observation geometries within short time windows, a promising data source for high temporal resolution and to improve the robustness of ionospheric reconstructions. This study introduces a novel framework to integrate sTEC data from ground-GNSS (from the International GNSS Service (IGS) network), ground-LEO (LEO-PNT), and LEO-GNSS (from Precise Orbit Determination antennas, POD) links for enhanced ionospheric reconstruction. Specifically, we model the logarithm of the 3D electron density using cubic B-splines at 15-min resolution. We employ an extended Kalman filter (EKF) with information filtering, rather than conventional least-squares adjustment, to enable rapid, robust temporal updates as required for real-time or near-real-time applications.

EKF-based approaches, by contrast to ART/MART or least-squares estimation, offer improved robustness in the presence of ill-posed geometries and singularities, thanks to their ability to propagate covariance and uncertainty, assimilate new data as it becomes available, and regularize the estimation process over time. Therefore, the inversion is less prone to artifacts, which can originate from non-observed or poorly observed basis functions, since their estimation is properly weighted with the parameter covariance matrix.

The study is conducted as a closed-loop simulation: sTEC is extracted from the IRI-20 model and used to estimate electron density model coefficients, with outcomes compared against IRI-20 reference values. The EKF updates the electron density maps every 15 min, with only the initial epoch initialized from IRI-20. Smoothing is applied to promote robustness and reduce outlier effects. The experimental design investigates the value of each sTEC data source (see Table 1), evaluating cases with various combinations of ground-GNSS, LEO-GNSS (POD), and ground-LEO (PNT) links.

The novelties of this study are the ionospheric reconstruction using an information filter based solely on relative observations and the inclusion of LEO-PNT data for a closed-loop simulation. This is done using non-ideal but realistic observation geometries obtained from an existing ground network and existing LEO satellites. We also use combinations of different data sources (ground-GNSS, LEO-POD, LEO-PNT). This distinguishes our work from Nikoukar et al. (2015b), where a 3D-var algorithm with COSMIC-POD was used, and the work from Prol et al. (2023), where ideal distributions of ground stations and LEO satellites is assumed for a voxel-based

Table 1
Experimental setup: "+" indicates inclusion, "-" exclusion of respective data sources.

Test	LEO-GNSS(POD)	ground-LEO (PNT)	ground-GNSS
100	+	-	-
010	-	+	-
001	-	-	+
110	+	+	-
101	+	-	+
011	-	+	+
111	+	+	+

reconstruction. A simulation to assess the contributions of different data sources has, to our knowledge, not yet been conducted.

The key aims are to quantify the improvement in ionospheric reconstruction with each additional data type and to identify at what point further data sources yield diminishing returns. We highlight the importance of radio occultations (RO) and how LEO-PNT can be used for improved spatial and temporal resolution.

2. Generation of synthetic data

Synthetic data are generated using the electron density from the IRI-20 model as input. The electron density along the line of sight between the transmitter and receiver is evaluated and numerically integrated to obtain the slant TEC. The International GNSS Service (IGS) provides GNSS satellite orbits for May and June 2020 (here, we use GPS and Galileo, Selmke et al. (2020)). For the LEO satellites, we utilize precise orbits from various processing centers (see Table 2). Satellite positions are sampled at a 30-s cadence. As a ground network, we use the IGS20 stations (https://network.igs.org/), comprising a total of 273 stations distributed worldwide. The station distribution is shown later in Fig. 6, where the local accuracy of the reconstructions is also discussed; additionally, a list of the stations, together with their coordinates, can be found in the supplementary material. In case a LEO or GNSS satellite is visible (with an elevation mask of 10 degrees), the line of sight between the ground station and the LEO or the ground station and GNSS satellite and the synthetic slant TEC are computed. The integration for slant TEC is done using the Gauss–Legendre quadrature. For LEO-GNSS and ground-GNSS, the ionosphere and plasmasphere are integrated separately, to keep the order of the Gauss–Legendre quadrature low, but still ensure sufficient accuracy. For ground-GNSS applications, the split was performed at 1000 km, with 15 support points below 1000 km and 10 support points above. For LEO-GNSS, the split was performed at 3000 km, with 10 support points below 3000 km and five support points above. In contrast, for LEO-PNT, no split was made, and 15 support points were used. For ground-GNSS and LEO-PNT links, we use all available links. In contrast, for LEO POD, the actual observed GNSS satellites as specified in the Receiver Independent Exchange (RINEX, Gurtner and Estey (2007)) observation file are used. In the case of COSMIC-2, this also includes occultation with elevations as low as −20 degrees concerning the local horizon.

Table 2
Sources for the precise orbit data of Low Earth Orbit (LEO) satellites used in this study. "AIUB" stands for Astronomical Institute, University of Bern; "ESA" is the European Space Agency; "GFZ" refers to the Helmholtz Centre Potsdam, German Research Centre for Geosciences (GeoForschungsZentrum); "UCAR" is the University Corporation for Atmospheric Research; "Sentinel-Hub" provides open data access for the Copernicus Sentinel satellites operated by ESA.

Satellite	Orbit source
Swarm	ESA (https://swarm-diss.eo.esa.int/)
GRACE-FO	GFZ RSO Orbit (ftp://isdcftp.gfz.de/)
Jason-3	AIUB (internally provided)
Sentinel	Sentinel-Hub (https://dataspace.copernicus.eu/data-collections/sentinel-data)
COSMIC-2	UCAR (https://data.cosmic.ucar.edu/gnss-ro/cosmic2/)
Spire	AIUB (internally provided)

3. Methodology

We model the electron density in logarithmic form, with the logarithmic electron density described globally by a cubic B-spline in magnetic latitude, mag. local time (LT), and altitude. This leads to the equation

$$log_b(Ne(mlat, mlt, h)) = \sum_{i,j,k} (B_i(mlat) \cdot B_j(mlt) \cdot B_k(h)) \cdot x_{i,j,k}, \tag{1}$$

where b is the selected basis of the exponential, B_i, B_j, and B_k are the basis functions in mag. latitude, mag. local time and altitude, and $x_{i,j,k}$ is the coefficient of the specific combination of basis functions. Here, the logarithmic electron density is given as the product of the basis functions, which are equally spaced in mag. LT and latitude, but denser in altitude near the F2 peak, around 350 km to 400 km altitude. More details are available in Schreiter et al. (2024). To recover the electron density from the TEC measurements, we employ an extended Kalman filter (Simon, 2006). It is essential to note that slant TEC measurements are highly precise, down to 0.01 TEC Units (TECU), considering only relative variations (Khodabandeh and Teunissen, 2016; Brack et al., 2021). However, uncertainties can reach several TECUs when estimating biases, particularly those associated with GNSS and receiver-specific effects. Our data assimilation scheme addresses the issue of leveling uncertainties by differencing each observation relative to the first observation within a 15-min time batch. To ensure reliability, observational arcs must be free of gross errors. Thus, in a real-world scenario, it is crucial to carefully identify and address potential critical issues such as gaps, cycle slips, or loss of lock during TEC processing.

The primary goal of data assimilation is to match the observed slant TEC (sTEC) with the modeled slant TEC for each arc. For that purpose, we need to integrate the electron density along the line of sight, which requires weights (w_i) depending on the quadrature formula and the electron density at the support points (Ne_i) for numerical integration. This can be written as

$$sTEC \approx \sum_{i=1}^{n} w_i Ne_i. \tag{2}$$

The sum and the weights can be summarized as a matrix (L), whereas the logarithmic electron density can be com-

puted by a matrix (D), which contains the values of the basis functions at the support points. D multiplied with the parameter vector x, it provides the logarithmic electron density, and taking the exponential with respect to the basis b, the electron density is obtained. Including arc-wise biases that originate from the sTEC estimation procedure, this can be written as

$$sTEC_{arc} \approx L \cdot b^{Dx} + B_{arc}, \tag{3}$$

where:

- $sTEC_{arc}$ is the vector containing slant TEC for a given arc,
- L is the integration matrix containing weights for the Gauss–Legendre quadrature,
- b is the basis of the exponential,
- D evaluates the B-spline basis at the support points given the coefficients x, depending on the basis functions and the position of the support points.
- B_{arc} contains all arc-wise constant biases.

To eliminate constant bias parameters, we recast this equation in a differentiated form:

$$sTEC_{arc} - sTEC_{arc}(t_0) \approx L \cdot b^{Dx} - L_0 \cdot b^{Dx}, \tag{4}$$

where L_0 is the first column of L. Since most of the entries of L_0 are zero, in theory, the computation of most of the entries of D could be omitted. However, since Dx must be computed for L regardless, these results can be reused directly.

3.1. Extended Kalman Filter as Extended Information Filter

Due to the presence of non-linearities in the system, we employ an extended Kalman filter (EKF) in the dual-form as extended information filter (Simon, 2006; Thrun et al., 2005). In this variant of the Kalman/information filter, a local linearization is performed at each update step. To further mitigate issues arising from non-linearities, we iterate the update step with an upscaled observation noise covariance matrix. This approach yields smaller update steps and repeated re-evaluation of the Jacobian matrix, thereby improving convergence in non-linear regimes. It is furthermore less prone to singularities, as they can arise from least-squares adjustment and can be implemented computationally efficiently, which will later be shown by decomposing the updates into arc-wise increments.

The key components of a Kalman filter are the state-vector x and the covariance matrix P, whereas for an information filter they are the information vector i and matrix I. They are directly linked by

$$I = P^{-1}, \tag{5}$$

$$i = Ix. \tag{6}$$

Both filters consist of a predict and update step. The prediction for timestamp $k+1$ given the previous state at timestamp k reads as

$$P_{k+1|k} = F^{\mathrm{T}} P_{k|k} F + Q, \tag{7}$$

$$x_{k+1|k} = F x_{k|k}. \tag{8}$$

Here, we use a fixed state transition matrix F, which performs anisotropic smoothing of the logarithmic electron density. The smoothing is enhanced along the direction of the geomagnetic field lines and is more restricted in the perpendicular direction, Q is a diagonal process noise matrix, here $Q = \mathbf{1}\sigma_0$.

In an extended Kalman filter, the update is performed by

$$P_{k|k} = (\mathbf{1} - K_k J_k) P_{k|k-1} \tag{9}$$

$$x_{k|k} = x_{k|k-1} + K_k(z_k - h(x_{k|k-1})), \tag{10}$$

where J_k is the Jacobian of the measurement function h, K_k is the Kalman gain, and z_k are the observations. The Kalman gain is defined as

$$K_k = P_{k|k-1} J_k^T S_k^{-1}, \tag{11}$$

with the residual covariance matrix

$$S_k = J_k P_{k|k-1} J_k^T + R_k, \tag{12}$$

where R_k is the observation covariance matrix.

In the extended information filter, being the dual of the extended Kalman filter (Thrun et al., 2005), the update is written as

$$I_{k|k} = I_{k|k-1} + \Delta I_{k|k-1} = I_{k|k-1} + J_{k|k-1}^T R_k^{-1} J_{k|k-1} \tag{13}$$

$$i_{k|k} = i_{k|k-1} + \Delta i_{k|k-1} = I_{k|k-1} + J_{k|k-1}^T R_k^{-1}(z_k - h(x_{k|k-1}) + J_{k|k-1} x_{k|k-1}). \tag{14}$$

In the case of R being a diagonal or a block-diagonal matrix, as is the case for assimilating observational arcs, $\Delta I_{k|k-1}$ and $\Delta i_{k|k-1}$ can be decomposed into a sum of arc-wise contributions.

$$I_{k|k} = I_{k|k-1} + \sum_{\text{arc}} \Delta I^{arc}_{k|k-1}, \tag{15}$$

$$i_{k|k} = i_{k|k-1} + \sum_{\text{arc}} \Delta i^{arc}_{k|k-1}. \tag{16}$$

with

$$\Delta I^{arc}_{k|k-1} = (J^{arc}_{k|k-1})^T (R^{arc}_k)^{-1} J^{arc}_{k|k-1} \tag{17}$$

$$\Delta i^{arc}_{k|k-1} = (J^{arc}_{k|k-1})^T (R^{arc}_k)^{-1} (z^{arc}_k - h^{arc}(x_{k|k-1}). \tag{18}$$

As outlined in Eq. (4), we differentiate against the first observation in each arc. This task can be performed using a reduction matrix M^{arc}_d, which is $n-1 \times n$ and reads as

$$M^{arc}_d = \begin{pmatrix} -1 & 1 & & 0 \\ \vdots & & \ddots & \\ -1 & 0 & & 1 \end{pmatrix} \tag{19}$$

.

Therefore, we define

$$z^{arc} = M^{arc}_d \cdot (sTEC^{arc}_0, \ldots, sTEC^{arc}_n)^T. \tag{20}$$

Following Eq. (4) the observation function H can be written as

$$h^{arc} = M_d^{arc} L^{arc} b^{D^{arc} x}. \tag{21}$$

Consequently, the Jacobi matrix reads as

$$J^{arc} = M_d^{arc} \cdot L^{arc} \cdot ln(b) \cdot b^{D^{arc} x} \cdot D^{arc}, \tag{22}$$

For an arc with n measurements ($n-1$ observations after differencing), the noise covariance matrix R_{arc} of size $(n-1) \times (n-1)$ is constructed as:

$$R_k^{arc} = \mathbf{I}_{n-1} \cdot \sigma + \sigma, \tag{23}$$

where σ is the noise of sTEC observations.

To better cope with non-linearity, the update step in the information-filter (13, 14) is iterated (here three times, with increased observational noise). In the case of the Kalman filter, the assimilation requires computing the Kalman Gain K (11), which requires inverting the residual covariance matrix S (12), which can be computationally expensive if the number of observations is large. In the information filter, this inversion is not required. If decomposed in relatively short arcs, the inversion of the (small) observation covariance R is fast. As long as they are independent, the computations can run in parallel, and the update using the sum of the arc-wise innovations $\Delta I^{arc}, \Delta i^{arc}$ can easily be computed.

The filter is initialized by performing a least-squares fit of the model parameters x_{IRI} to the IRI-2020 model with the cor2 topside option:

$$x_0 = x_{\mathrm{IRI}}, \tag{24}$$

$$P_0 = \mathbf{1}\sigma_0, \tag{25}$$

where the initial parameter covariance matrix P_0 is a diagonal matrix with fixed variance σ_0. Using Eq. 5 we obtain I and i for the information filter formulation.

4. Results

For our investigation, we used a relatively coarse resolution with 19 basis functions in mag. latitude, 12 in mag. LT, and 11 in altitude. The spacing of the cubic B-Splines is two hours in mag. LT, 12 degrees in mag. latitude, and in altitude using control points at 80 km, 200 km, 350 km, 500 km, 1000 km, 5000 km, and 22000 km, which allows for more variation in low altitudes and near the F2-peak. Reconstructions were performed for all cases outlined in Table 1. The first epoch was initialized using the IRI 2020 model. All subsequent epochs are the output of data assimilation. We also perform a zero-test (000), where only the forward model is run without assimilating data to judge which variations are data-driven and which dynamics originate from the prediction step alone. The tests were carried out in May 2020 under solar minimum conditions. The Kalman Filter was initialized on May 1, 2020, at 00:00:00 UTC and ran until May 4, 2020, at 23:45:00 UTC. We consider solar minimum conditions to be particularly challenging because the signal in slant TEC is weakest. Since the source of the synthetic slant TEC is a climatological model, we do not investigate fast temporal and small-scale fluctuations or storm-time responses. The quality assessment of the reconstructions was done using synthetic electron density observations from the Swarm (near 500 km altitude), GRACE-FO (near 500 km altitude), and DMSP (Defense Meteorological Satellite Program (Rich, 1994), near 850 km altitude) locations. They carry instruments to measure electron density and could therefore be used when using real data. We will further investigate the relative differences on a global grid at altitudes between 100 km and 2000 km. We evaluate the global error with respect to altitude for the tests listed in Table 1. An exemplary three-dimensional electron density obtained from the reconstruction using all three data sources, namely ground-GNSS, Ground-LEO, and LEO-GNSS, is shown in Fig. 1.In the top row of the figure the IRI-2020 electron densities and in the bottom row the reconstructed electron densities are shown. It may be recognized on the left-hand side that, apart from low altitudes (near 150 km) and near 00:00, only minor differences in electron density are visible. The increased errors in reconstructing electron density near midnight are on the one hand due to low electron densities and consequently a low signal in sTEC, but on the other hand also by the observational geometry, where mostly the LTs near 06:00 LT and 18:00 LT are sounded. Additionally, observational gaps occur around 00:00 LT and 12:00 LT off the geomagnetic equator, where observations are provided exclusively by the COSMIC-2 constellation (see Fig. 2).

4.1. Local electron density comparison

The electron density is evaluated locally at the positions of Swarm A, Swarm B, Grace-FO, and DMSP-F18. We omit Swarm C because of the close proximity to Swarm A, since no significant differences are expected. Swarm (Lomidze et al., 2018) and DMSP (Rich, 1994) carry Langmuir probes and are therefore capable of measuring the electron density directly. In contrast, for GRACE-FO, the electron density is approximated using the inter-satellite K-Band ranging system (Schreiter et al., 2023). In a real-world scenario, these satellites would be used to validate the reconstruction, as it was done in Schreiter et al. (2024). Here, we compute electron density for the satellite positions of those missions from the IRI-20 model and, consequently, can neglect calibration biases that may occur in reality (e.g., Pakhotin et al. (2022)). An example of the comparison between Swarm A, DMSP-F18, and the reconstruction for tests 100, 110, 011, and 111 (see Table 1) is shown in Fig. 3. The relative percent difference is defined as

$$\epsilon_{rel} = 2 \cdot \frac{Ne_{IRI} - Ne_{Mod}}{|\, Ne_{IRI} + Ne_{Mod} \,|}, \tag{26}$$

where Ne_{IRI} is the IRI electron density and Ne_{Mod} is the modeled electron density. During the time span presented in the comparison, Swarm-A was near 07:10/19:10 LT at a mean altitude of 444.84 km, while DMSP-F18 was near

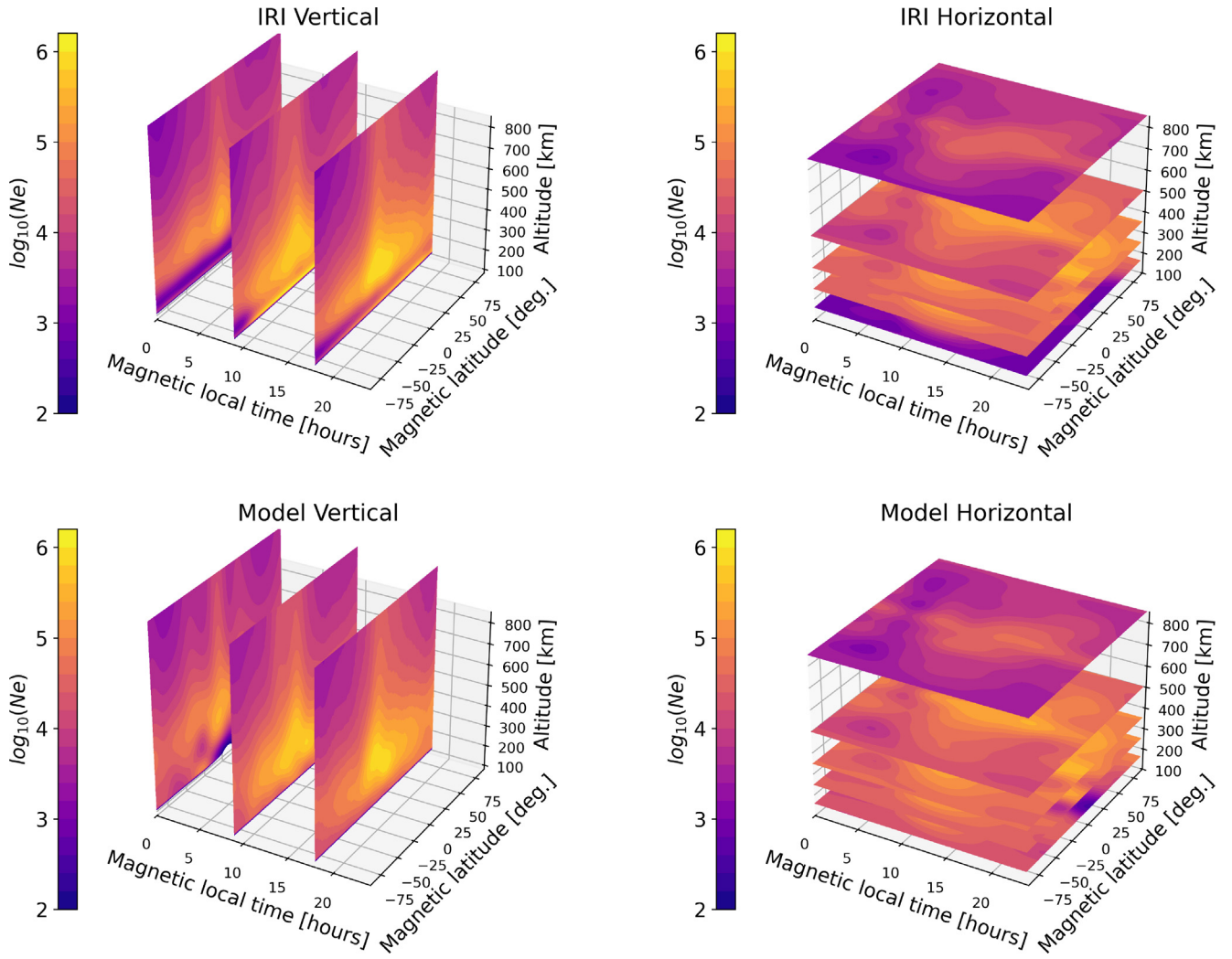

Fig. 1. Vertical (left) and horizontal (right) slices of electron density for the IRI-2020 model using cor2 topside (top) and the reconstructed electron density (bottom) for 4th of May 2020, 12:00 UTC. Vertical slices are evaluated at 00:00 LT, 09:00 LT, and 18:00 LT, horizontal slices at 160 km, 250 km, 350 km, 500 km, and 850 km.

07:00/19:00 LT at a mean altitude of 857.5 km. The comparison with DMSP is of particular interest, since no slant TEC data were simulated for DMSP. It can be recognized that the densities in all cases follow the IRI densities. In the case of Swarm, the peaks are generally well represented, with the largest relative errors occurring in case 011 and in cases where no radio occultation data (here, sTEC with negative elevation) were included (No RO). For DMSP, the importance of including POD observations becomes more evident, since the 011 test without POD data cannot compete in terms of relative error. Furthermore, one can see some discrepancies near sunrise, which originate from lower altitudes, propagate to higher altitudes, and are caused by the limited resolution of the B-Splines.

A more extensive comparison is performed in Fig. 4. Here, we evaluate the electron densities for Swarm A/B/C and GRACE-FO at altitudes near 500 km (left side) and DMSP-15/16/17/18 at altitudes near 850 km (right side). The time period for comparison is from May 2nd to May 5th, with May 1st excluded because the first epoch of that day is used to initialize the Kalman Filter. The top row shows the 000 case, where no data is assimilated, and only the forward model (identity with smoothing) is run. Figures showing the other comparisons can be found in Appendix A. A Full listing of the correlations and the RMSE is shown in Table 3.

A peculiarity is already evident in this comparison. The test 110 and 111 both show an excellent correlation of 0.99; however, surprisingly, the Root Mean Squared Error (RMSE) of test 110 is $9.5 \times 10^3 cm^{-3}$ near 500 km, and $1.58 \times 10^3 cm^{-3}$ (near 850 km), while for test 111 it is $11.2 \times 10^3 cm^{-3}$ near 500 km, and $1.91 \times 10^3 cm^{-3}$ near 850 km. Therefore, one might judge that the ground-GNSS links do not provide significant additional information and can even weaken the reconstruction. They increase the error since observational and integration errors are pushed to weakly determined locations. Those are in the along- and cross-track direction of the LEO satellites, since the LEO-POD constrains the upward-looking cone and LEO-PNT constrains the downward-looking cone. The

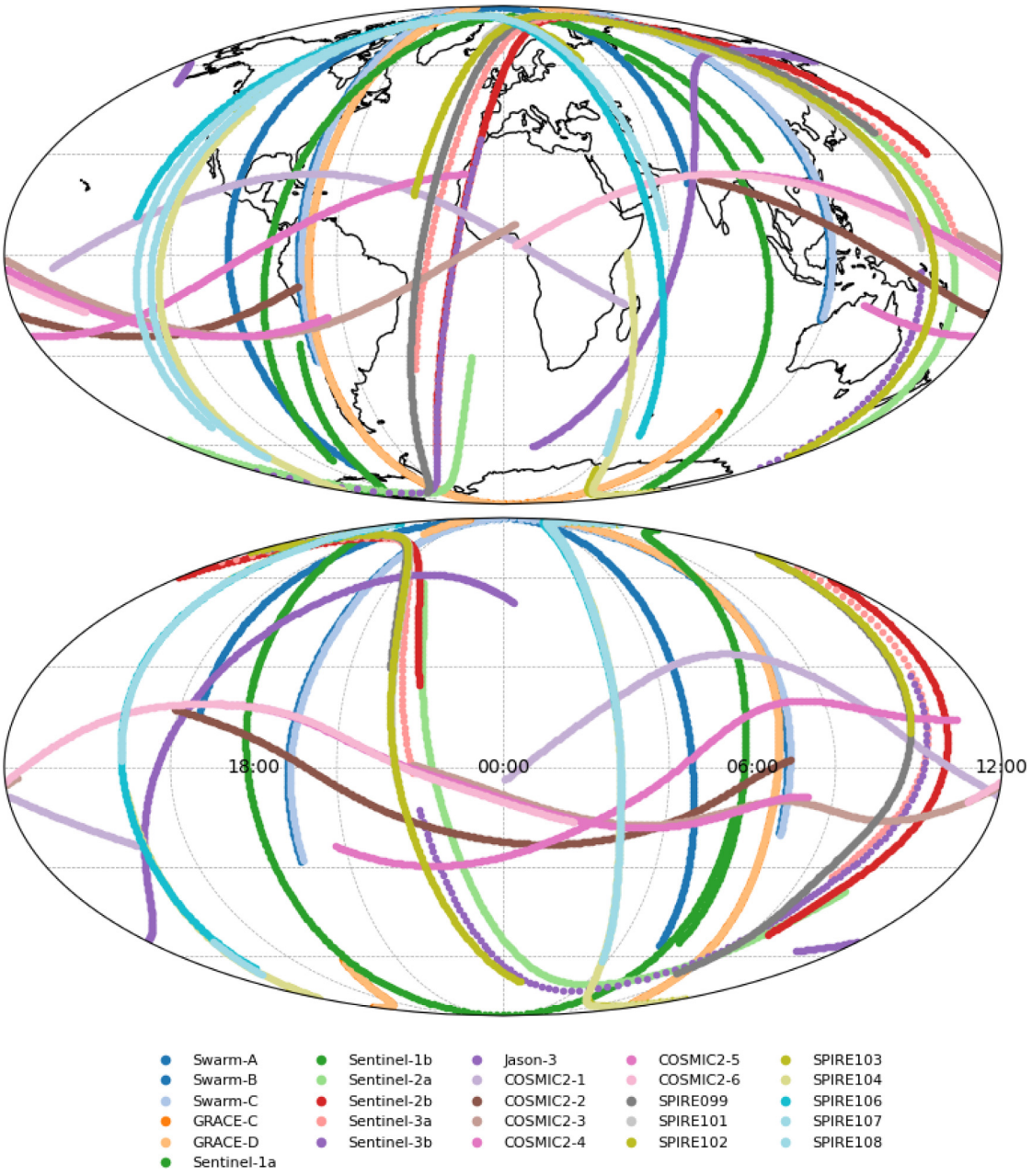

Fig. 2. Ground tracks of the satellites used between 11:00 UTC and 12:00 UTC on 4th of May 2020 in geographic coordinates (top) and magnetic latitude and LT (bottom).

horizontal component is only constrained by COSMIC-2 RO data. Compared to test 101 (without PNT), which shows an RMSE of $11.8 \times 10^3 cm^{-3}$ near 500 km and $1.87 \times 10^3 cm^{-3}$ near 850 km, one can also conclude by comparing to test 110 that PNT data strengthen the reconstruction. Furthermore, ground-GNSS links alone cannot replace LEO-POD or LEO-PNT data. The plot for test 011 can be found in the Appendix. Here, a degradation can be observed, with the RMSE increasing to $40.3 \times 10^3 cm^{-3}$ near 500 km and $4.72 \times 10^3 cm^{-3}$ near 850 km, respectively. The figures for single data-source observation scenarios, namely tests 100, 010, 001, and the No RO cases, are also included in the Appendix.

4.2. Global reconstruction with respect to altitude

To evaluate the quality of the reconstruction on a global scale with fixed altitudes, we used a regular grid in mag. latitude (3-degree spacing) and in mag. LT (00:30 h spacing). For each grid point, we compute the electron density according to IRI for each test scenario. For quality assessment, we compute the RMSE and compare it to the RMSE of test 000, where only the forward model is run. The relative RMSE (RMSE of the test divided by the RMSE of test 000) is expressed in percent, where a relative RMSE of 100% means that the reconstruction is as good as or as bad as the forward model; a relative RMSE below

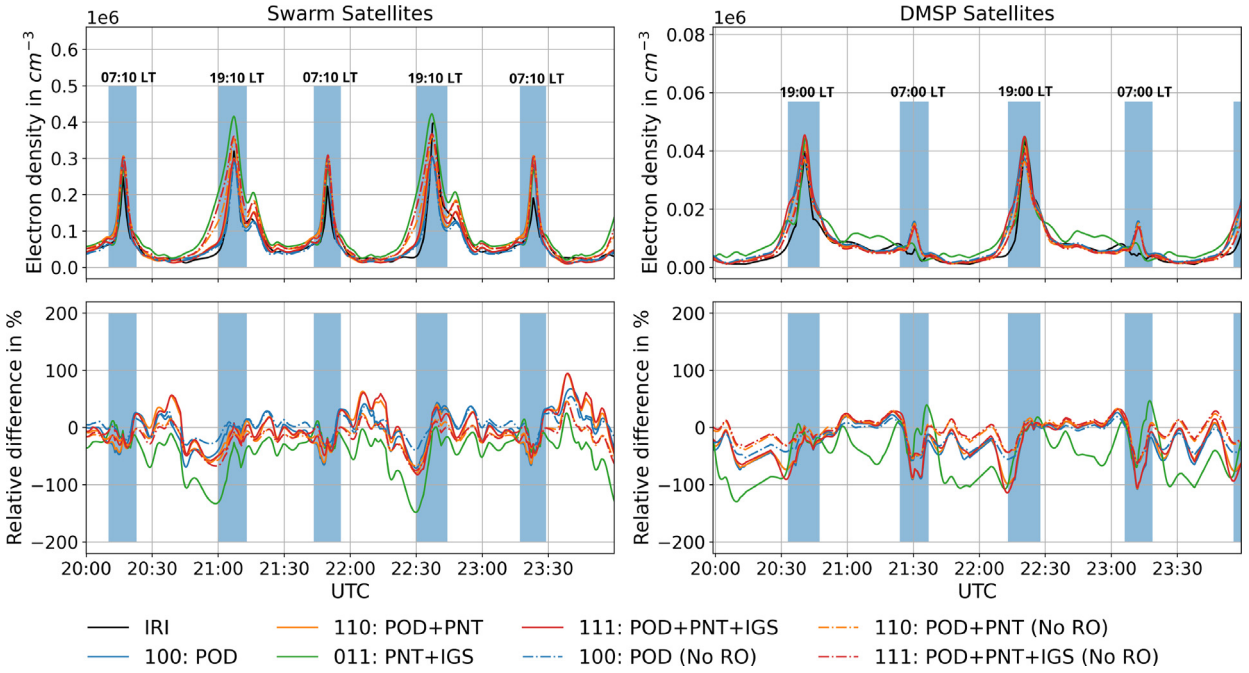

Fig. 3. Comparison of reconstructed electron densities for tests 100, 110, 011, and 111, with negative elevation from COSMIC-2 and without (No RO). Blue shaded areas indicate the equatorial crossings ($\pm 20°N$). Densities are plotted in the top figure, and the relative error is plotted in the bottom figure. On the left side, the comparison is carried out for Swarm A, on the right side for DMSP-F18.

100% indicates an improvement, and a relative RMSE above 100% indicates a degradation. The comparisons are also carried out from 2 May 2020 00:00:00 UTC until 4 May 23:45:00 every 15 min. The statistics of the relative RMSE for the entire timespan are shown as boxplots. The results are shown in Fig. 5, grouped by altitude. We selected tests 110, 101, 011, 111, and 111 (No RO). The remaining tests are presented in Appendix B.

In Fig. 5, it is evident that test 011, which combines LEO-PNT and ground-GNSS, begins to degrade severely above altitudes of 400 km. However, for altitudes between 100 and 300 km, a reduction of the relative RMSE to 40% is observed at 300 km, showing an improvement in low altitudes. Test 111 without RO shows a pronounced degradation at 400 and 500 km. All other altitudes generally show an improvement, which, especially at low altitudes, is weaker than for the remaining tests. Test 110 reduced the relative RMSE by more than 50% (apart from an altitude of 2000 km) and is usually among the best, similar to test 111. The altitude near 100 km is probably affected by gaps in the ground network. Test 101 performs similarly to test 110 and test 111; especially, altitudes near the F2 peak at 400 km seem to be degraded. Still, even here, an improvement of almost 50% is achieved for most altitudes. Data from the POD antenna appears to be essential for topside monitoring (altitudes above 400 km), as can be seen by excluding them in test 011 results in a degradation above that altitude. RO observations are also proven to be essential, since excluding them (test 111 (noRO)) results in a clear degradation near 400 km and 500 km.

4.3. Localization of improvements

The irregular ground network and the unevenly distributed LEO orbits can affect the quality of reconstruction. Low background electron density can also affect the reconstruction, as low densities only provide a weak signal in sTEC. To investigate this assumption, we analyze the correlation between IRI-2020 and the model output at a selected height of 300 km. This altitude is not sounded by the LEO-POD antennas. We select the test cases 110 (POD + PNT), 101 (POD + IGS), 111 (POD + PNT + IGS) and 001 (IGS only) to investigate the benefit of LEO-PNT over IGS. We use a regular grid as in the previous section. As indicator we use the bin-wise Pearson correlation coefficient between IRI and the model electron density from 15 min reconstructions from 2nd of May until 5th of May 2020. The ground station network is plotted in red to illustrate the dependency of the correlation on the station distribution. The results are shown in Fig. 6. It can be observed that the smallest correlation occurs near areas where either the ionization is typically weak, or especially over the southern ocean and the Pacific, where only a few ground stations are located. The correlation may drop to roughly 0.5. For test 001 the weakest correlation is observed, with issues where no ground station are present, in the polar regions and near the geomagnetic equator. The deviations near the geomagnetic equator suggest, that the height dependency can not be well resolved when only using ground-stations. When comparing test 001 to test 101 where the POD observations were used in addition,

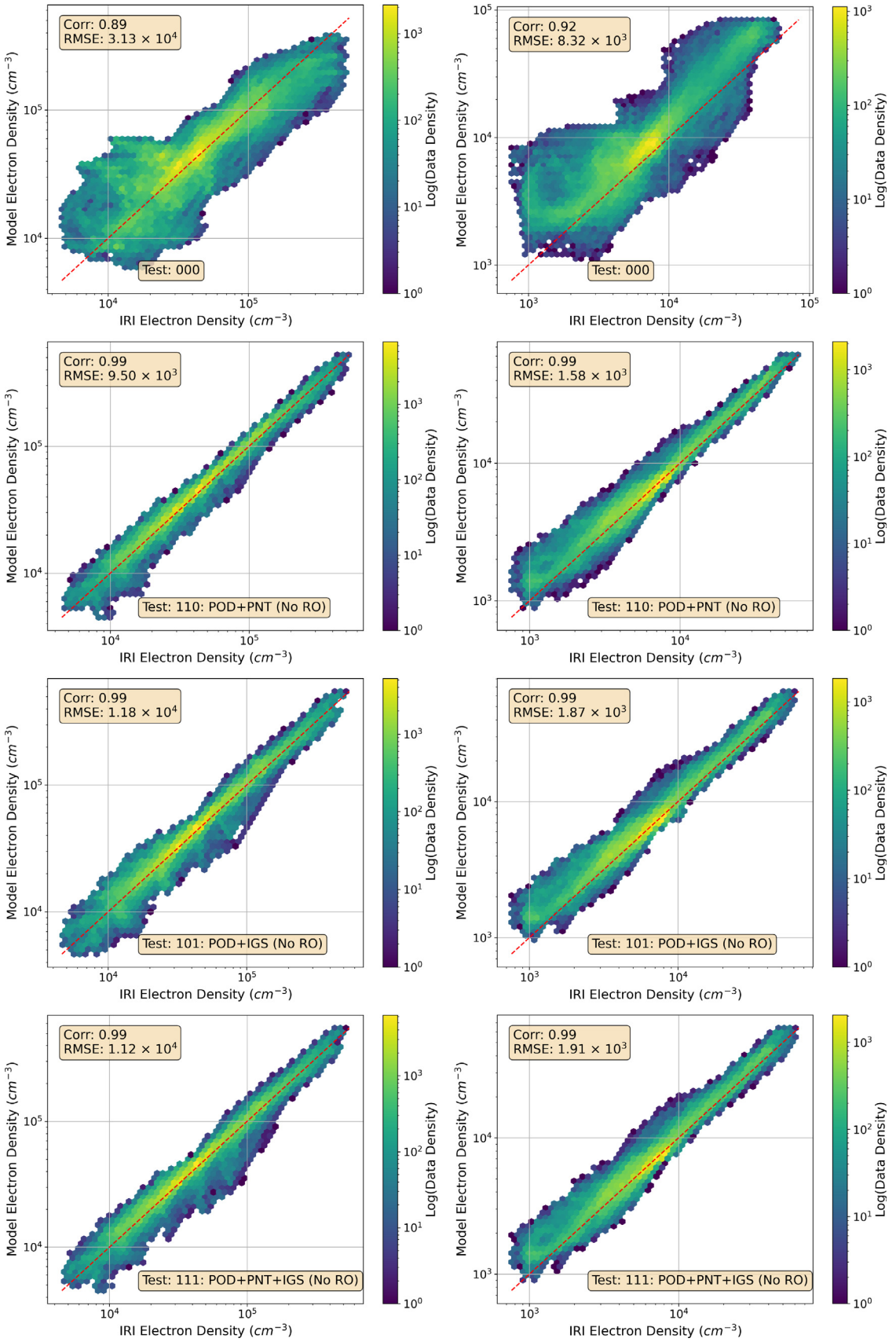

Fig. 4. Correlation plots for the different tests in logarithmic scale. IRI electron density is shown on the x-axis, whereas the modeled electron density is shown on the y-axis.

Table 3
Correlation and RMSE values near 800 km and 500 km for all investigated tests. Cell background colors indicate gradations of performance: **darker green** denotes optimal correlation ($\geqslant 0.99$) or lowest RMSE ($\leqslant 2 \times 10^3$ near 800 km, $\leqslant 1 \times 10^4$ near 500 km); **lighter green** indicates very good results (correlation 0.93–0.98, RMSE: 1.5×10^3–2×10^3 near 800 km, 1×10^4–1.2×10^4 near 500 km); **yellow** marks intermediate performance (correlation 0.89–0.92, RMSE: 2.0×10^3–5×10^3 near 800 km, 2×10^4–3×10^4 near 500 km); **darker red** highlights the poorest values (correlation $\leqslant 0.70$, RMSE $\geqslant 8.5 \times 10^3$ or $\geqslant 5.0 \times 10^4$); while **lighter red** indicates poor but not the worst outcomes.

	Correlation		RMSE in cm^{-3}	
	near 800 km	**near 500 km**	**near 800 km**	**near 500 km**
000	0.92	0.89	8.32×10^3	3.13×10^4
001: IGS	0.70	0.93	8.79×10^3	5.07×10^4
010: PNT	0.89	0.96	4.32×10^3	3.41×10^4
011: PNT+IGS	0.90	0.94	4.72×10^3	4.03×10^4
100: POD	0.99	0.99	1.83×10^3	0.85×10^4
100: POD (no RO)	0.99	0.99	1.38×10^3	1.11×10^4
101: POD+IGS	0.99	0.99	1.87×10^3	1.18×10^4
101: POD+IGS (no RO)	0.99	0.97	1.48×10^3	2.62×10^4
110: POD+PNT	0.99	0.99	1.58×10^3	0.95×10^4
110: POD+PNT (no RO)	0.99	0.98	1.13×10^3	2.20×10^4
111: POD+PNT+IGS	0.99	0.99	1.91×10^3	1.12×10^4
111: POD+PNT+IGS (no RO)	0.99	0.97	1.54×10^3	2.65×10^4

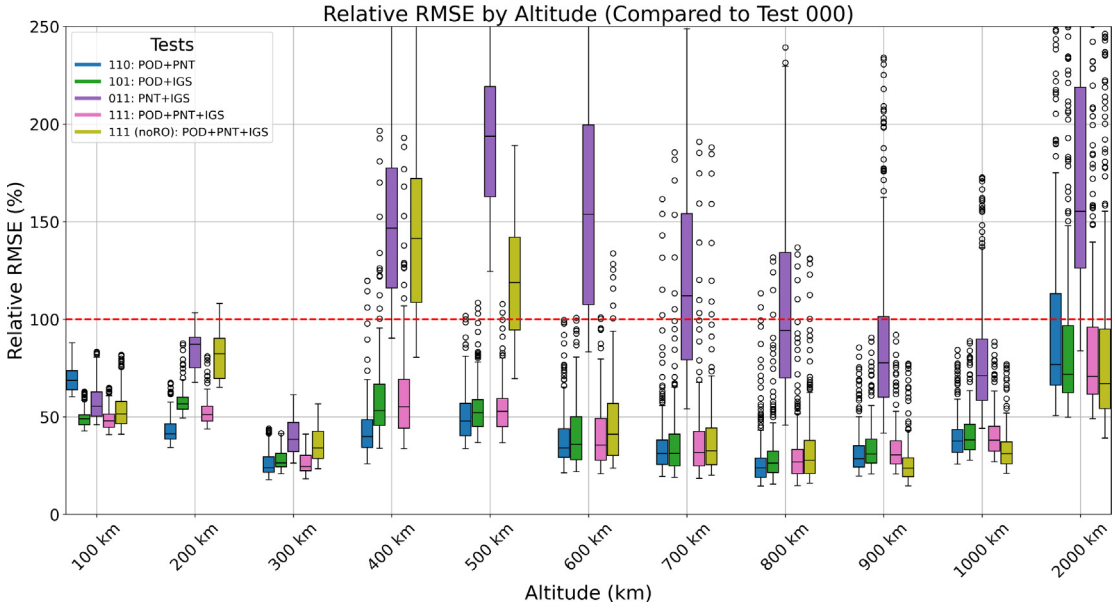

Fig. 5. RMSE with respect to IRI relative to test 000 evaluated on a global grid for tests 110, 101, 011, 111, and 111 (No RO). Provided as a boxplot with the size of the box being the inter-quartile range, the whiskers extending up to 1.5 times the inter-quartile range, and values outside the whiskers are plotted as circles.

one may see an improvement. In the equatorial band this improvement can be related to COSMIC-2 and the sTEC from negative elevations, but it can also be related to the improved altitudinal resolution. When excluding negative elevations from POD, the geomagnetic equator is visible, but less prominent, the corresponding figure may be found in the appendix. In test 101, the off-equatorial correlations also improve. Most prominently near point Nemo (Southern hemisphere near 120° W), but also over the oceans in the northern hemisphere in mid latitudes. Including PNT measurements (test 111), one may see, that the areas with lower correlations become smaller. The best overall correlation is achieved in test 110, where the lowest correlation is now near 0.7, again near point Nemo. In these comparisons, it is shown that including gound-GNSS in addition does not lead to an improvement. PNT, however, is shown to be responsible for most of the improvement. We conclude that this spatial improvement is achieved by the fast-changing ray geometry of PNT compared to ground-GNSS links, that do provide more signal in sTEC.

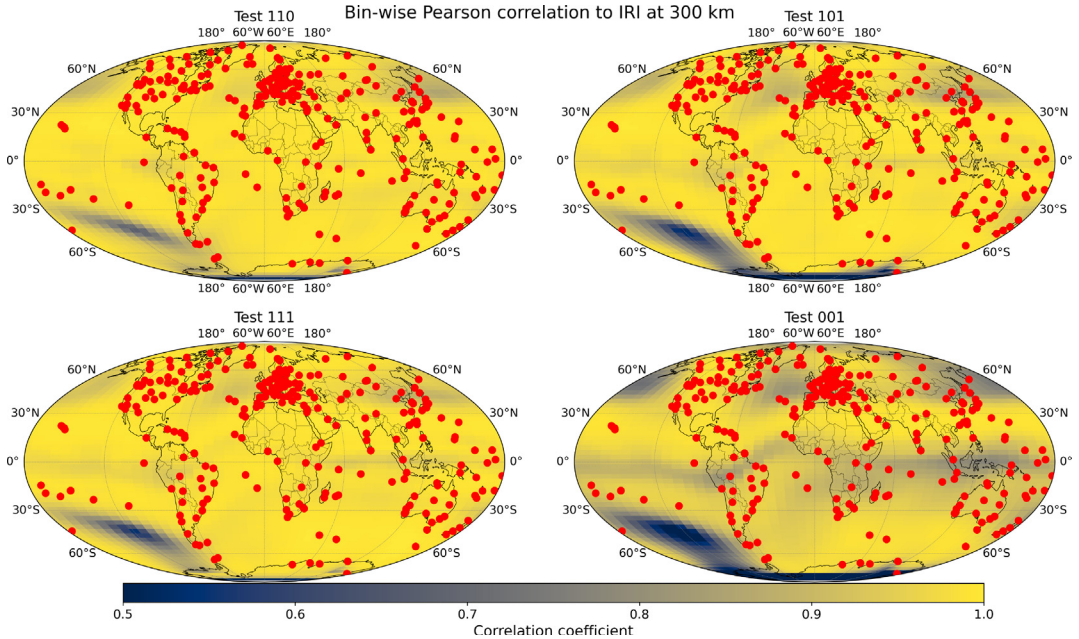

Fig. 6. Regionally binned correlation between IRI values and the model outputs at 300 km altitude. The coordinates of the used ground station are plotted in red. The comparison includes the cases 110 (PNT + POD), 101 (POD + IGS), 111 (POD + PNT + IGS), and 001 (IGS only).

5. Discussion

To monitor three-dimensional electron density, LEO-POD and the upcoming LEO-PNT satellites(ESA, 2025) are essential for improving the spatial and temporal resolution. Similar studies have already been conducted. In Prol et al. (2023), a constellation of 5700 LEO satellites was proposed in altitude planes of 250 to 850 km with 50 km spacing. In this study, we utilized only 26 satellites, whose orbital planes are defined by their mission requirements and cannot be considered optimal for ionospheric reconstruction. Furthermore, we utilized the locations of the existing IGS ground network, whereas in Prol et al. (2023), an optimal distribution of the ground stations was considered for a grid of voxels with $2^\circ \times 2^\circ$ resolution in latitude and longitude, and 10 km in altitude. The resolution in our study is much coarser, with approximately 12° in magnetic latitude and 2 h in LT, which corresponds to approximately 30° in longitude[1]. The essential differences are in the reconstruction method and the design of the basis function. Where Prol et al. (2023) used voxels with constant electron density, we describe the logarithmic electron density using B-splines, ensuring a smooth Chapman- or Epstein-like transition. Furthermore, integration is done differently, and the reconstruction method in Prol et al. (2023) is an algebraic reconstruction method based on voxels. In contrast, we employ an iterative Kalman filter, which also enables us to account for geometric issues and to constrain poorly or unobserved coefficients. In \citet{SchreiterIonLS}, a least-squares approach with constraints to account for those singularities was used. To solve arc-wise biases and avoid singular parameters longer observational arcs were required.Additionally, the Kalman filter approach is significantly faster, taking around 3:30 min for one 15-min time step on a standard PC (16 cores, 32 GB RAM) when utilizing all available data (test 111), and only 15 s when using LEO-POD and LEO-PNT (test 110).

In Nikoukar et al. (2015a), a 3D-var-based ionospheric reconstruction was performed. Six COSMIC satellites were used, along with numerical integration along the line of sight using a regular grid. Here, the grid was 5° in latitude and 10° in longitude. The altitudinal spacing was 200 km from 800 to 3000 km and 1000 km up to 20,000 km; low altitudes are not mapped. In their study, they used parameter constraints, which in our reconstruction are implemented via the background model (identity and smoothing) and parameter noise matrix. In contrast to their study, we employ a different parameterization by using B-Splines to model the logarithmic electron density instead of electron density directly on a grid. Additionally, we implemented an extended Kalman filter to accommodate a non-linear observation scenario. In contrast to both studies, we work with relative slant TEC observations only, as we consider calibration biases for absolute TEC at the level of the expected maximum signal, particularly for high-flying satellites. This modification is implemented by adapting the observation operator. Compared to reconstruction methods based on voxels, a constant electron density inside one voxel is not required. Additionally, methods using the algebraic reconstruction technique or similar approaches Bust and Mitchell (2008); Stolle et al. (2006); Heise et al. (2002); Gerzen and Minkwitz (2016) usually require a good observation geometry. If no good coverage of the voxels is given, they might show unrealistic values. Furthermore, those reconstruction methods usually work with absolute slant TEC and not with relative slant TEC. In this study, we bypassed the need for absolute TEC or estimating calibration biases by using dif-

[1] Tests were also carried out with approx. 6° in LT and 1 h spacing in LT. Because this study relies on large-scale synthetic data and multiple tests were compared, we kept the coarse resolution.

ferences. We also removed the constraint of representing an Epstein or Chapman Layer. As was recently shown by Prol et al. (2022), the topside does not necessarily follow the profile formulations and may have varying scale heights. Major outcomes of this study are, that when working with relative slant TEC only, near-horizontal or occulting measurements cannot be omitted. The reconstructions require their additional input. We conclude that they are essential for determining the absolute offset of relative slant TEC. It is also observed that for a fast time resolution (15 min compared to one hour TEC maps), the ground-based observation lacks information. This is prominent when looking at the spatial correlation, where the solutions including PNT show the best correlation, and the addition of ground-based observations does not make a significant difference. Even worse, the solutions tend to degrade when ground-GNSS links are used in addition. The cause might be, that the variation in slant TEC is small compared to variations that can be observed from LEO due to the fast change in observational geometry.

6. Conclusions

We developed a three-dimensional reconstruction framework that works with 15-min time batches of relative slant TEC observations. The study examines the impact of various observation tests and their combinations, specifically LEO-POD data, LEO-PNT data, and ground-based TEC. It has been demonstrated that the reconstruction is capable of reproducing the electron density with a correlation coefficient of 0.99 (test 111) and a reasonably low RMSE of approximately 1.91×10^3 cm^{-3} at 800 km and 1.12×10^4 cm^{-3} at 500 km. The test only including LEO-PNT and LEO-POD arcives also a correlation of 0.99, but even better RMSE of 1.58×10^3 cm^{-3} at 800 km and 0.95×10^4 cm^{-3} at 500 km. By comparing the reconstructions, we observed an apparent degradation near COSMIC-2 altitudes when radio occultation measurements (here used as slant TEC rather than as a density profile) were excluded. We conclude that the weakened observational geometry causes this effect, since without radio occultation, only observations near the LEO satellite positions are available. That limitation allows modeling and integration errors from ground-based TEC to propagate to altitudes with the largest gaps in sampling, which are the altitudes of the LEO satellites. This can be supported by test 011, which showed a degradation below the quality of the simplistic background model above 400 km up to plasmaspheric heights. We also found that test 110 (without ground-based slant TEC) did not perform worse than test 111, despite the latter using significantly more data. We assume that there are three main reasons: observational geometry, relative offset, and the little variation of ground-based slant TEC within a 15-min time window. In the assimilation, an arc with little or no variation is a nearly constant value. Since the adjustment relies on the time difference of TEC and geometry changes, an arc with only little variation in geometry holds only little information. For a near-real-time reconstruction, two criteria must be met. First, the processing strategy must be capable of near-real-time processing, which is realized using the information filter. Second, the data must hold the required information, which is provided by the fast-changing geometries of POD and PNT. The key conclusions are thus:

- LEO-PNT observations in addition to LEO-POD observations allow for a near-real-time reconstruction of the ionosphere and partly the plasmasphere (if the ionization is sufficiently high). Since we only use relative observations, sufficient variation in TEC over a short period (here 15 min) is required, which can be provided by LEO-PNT and LEO-POD.
- Relative slant TEC from ground stations can neither replace LEO-PNT nor LEO-POD observations. But vice versa, LEO-PNT and LEO-POD in combination can make ground-GNSS links redundant.
- All reconstruction tests suffer in case no low, or even negative (down to $-20°$) elevation data is available. Currently, only COSMIC-2 provides such data, which has been found essential for a reliable reconstruction.
- The unevenly distributed ground network poses limitations in the reconstructions for both LEO-PNT and ground-GNSS. LEO-PNT can partly compensate by fast changes in geometry. Additionally, the uneven distribution of ground stations can be partly compensated for by using radio occultation data, but those are only available in equatorial regions for COSMIC2 due to the orbital inclination of 24°.

The upcoming ESA LEO-PNT mission will initially consist of 10 satellites. They are planned to fly at an altitude of 500–600 km (ESA, 2025). An even distribution in LT would certainly help for ionospheric studies. With their launch, a three-dimensional ionospheric map would be required to correct for the ionospheric signal content in single-frequency applications accurately. Single-layer models are not suited for LEO-PNT, since the absolute slant TEC needs to be computed from the ground to LEO-PNT exclusively, without any contribution from LEO-PNT to GNSS. Eventually, the LEO-PNT mission will provide the opportunity to perform the reconstruction on real data.

Declaration of competing interest

The authors declare that they have no known competing financial interests or personal relationships that could have appeared to influence the work reported in this paper.

Acknowledgments

This work is part of the DFG HOLMES project, Grant No. 471275159.

Appendix A. Appendix A

Figs. 7 and 8.

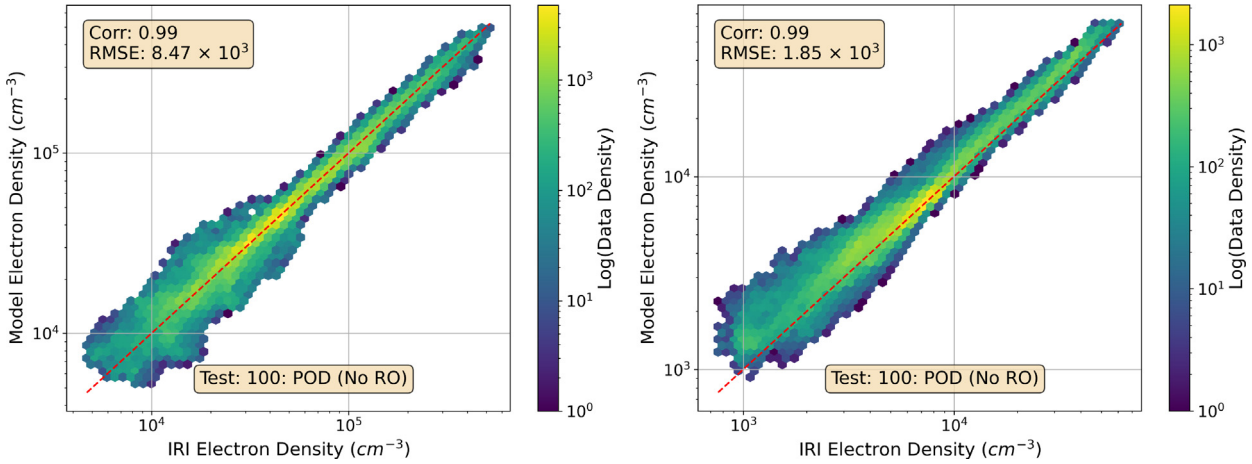

Fig. 7. Same as Fig. 4, but for test100.

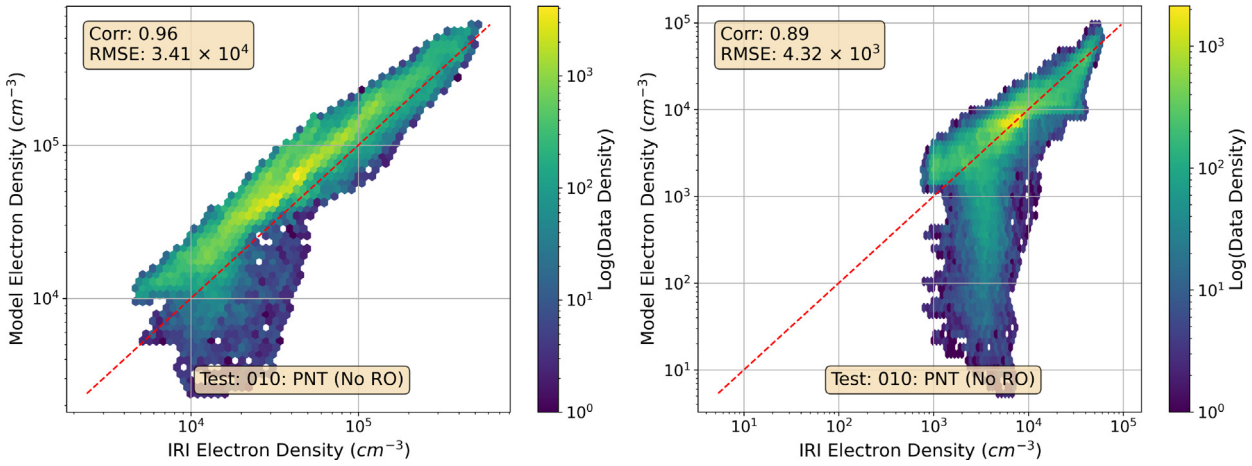

Fig. 8. Same as Fig. 4, but for test 010.

Appendix B. Appendix B

Figs. 9–16.

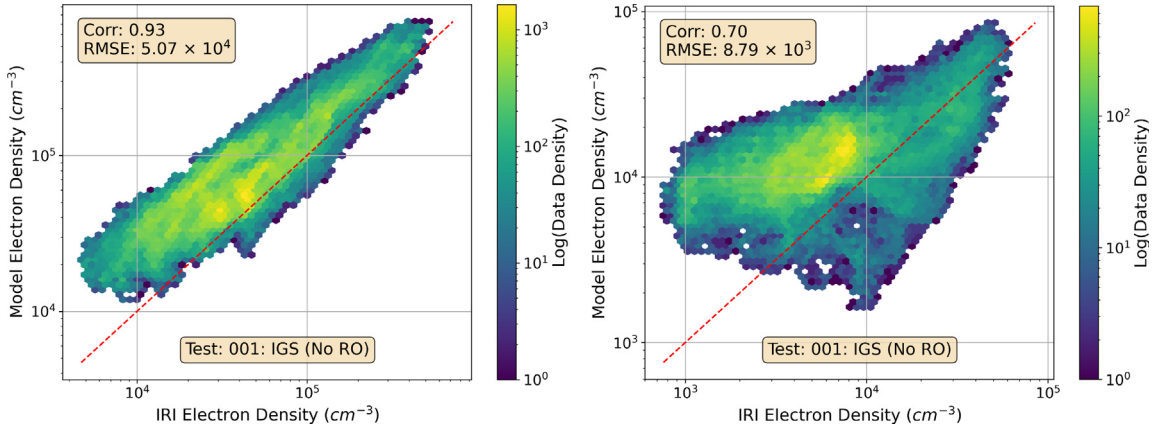

Fig. 9. Same as Fig. 4, but for test 001.

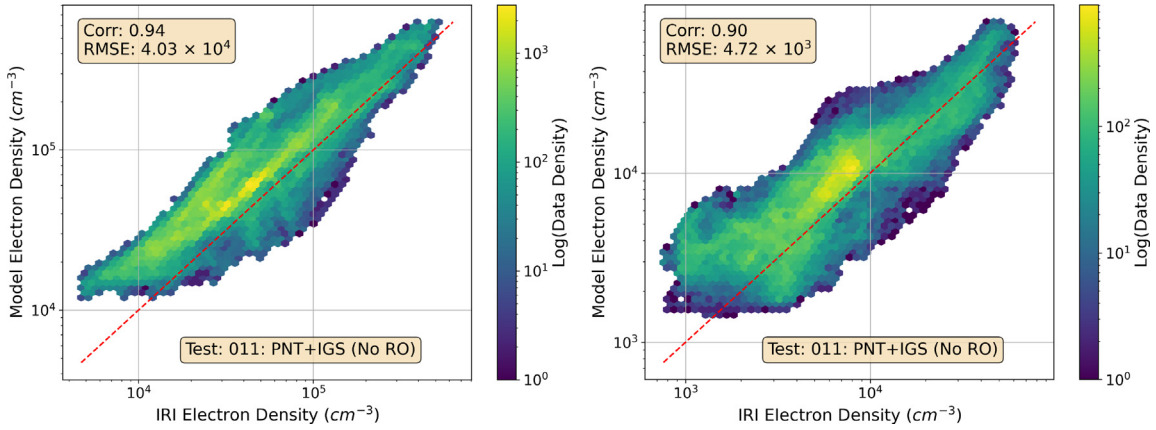

Fig. 10. Same as Fig. 4, but for test 011.

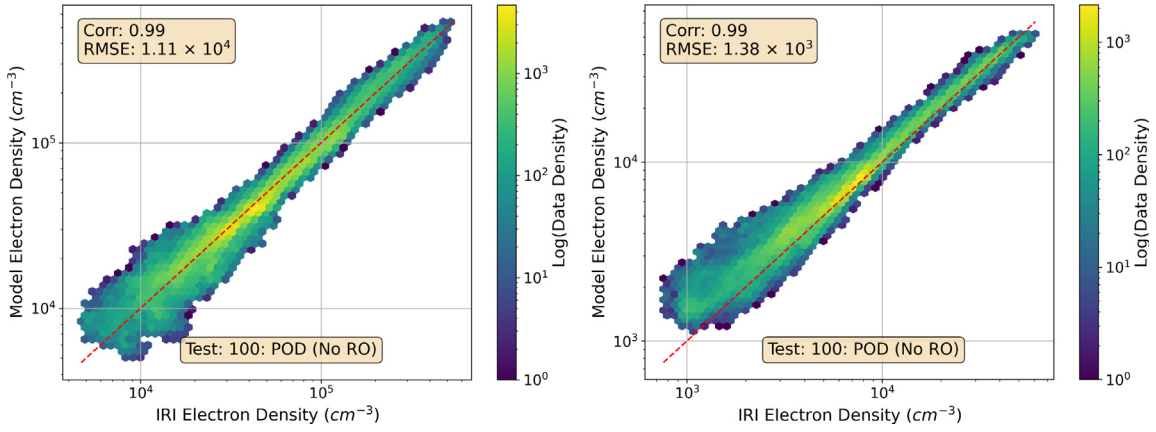

Fig. 11. Same as Fig. 4, but for test 100 (no RO).

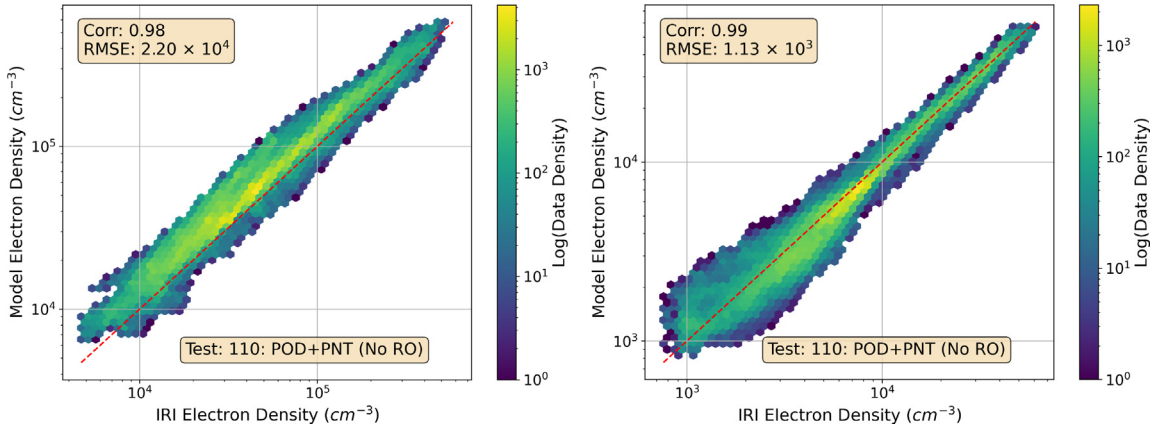

Fig. 12. Same as Fig. 4, but for test 110 (no RO).

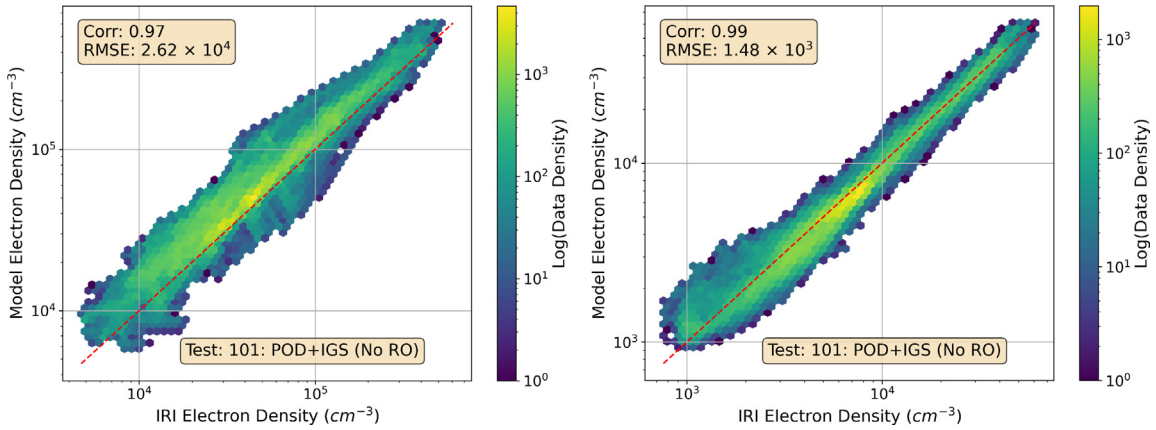

Fig. 13. Same as Fig. 4, but for test 101 (no RO).

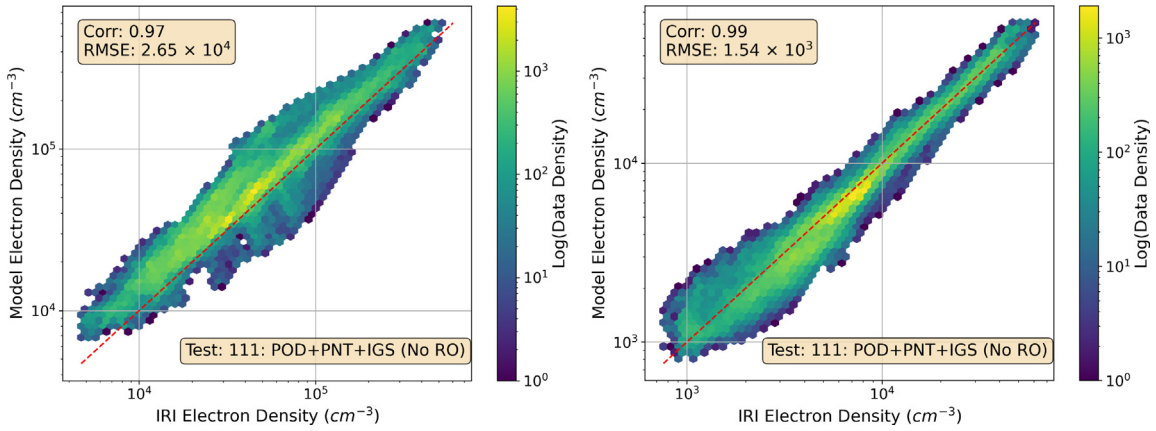

Fig. 14. Same as Fig. 4, but for test 111 (no RO).

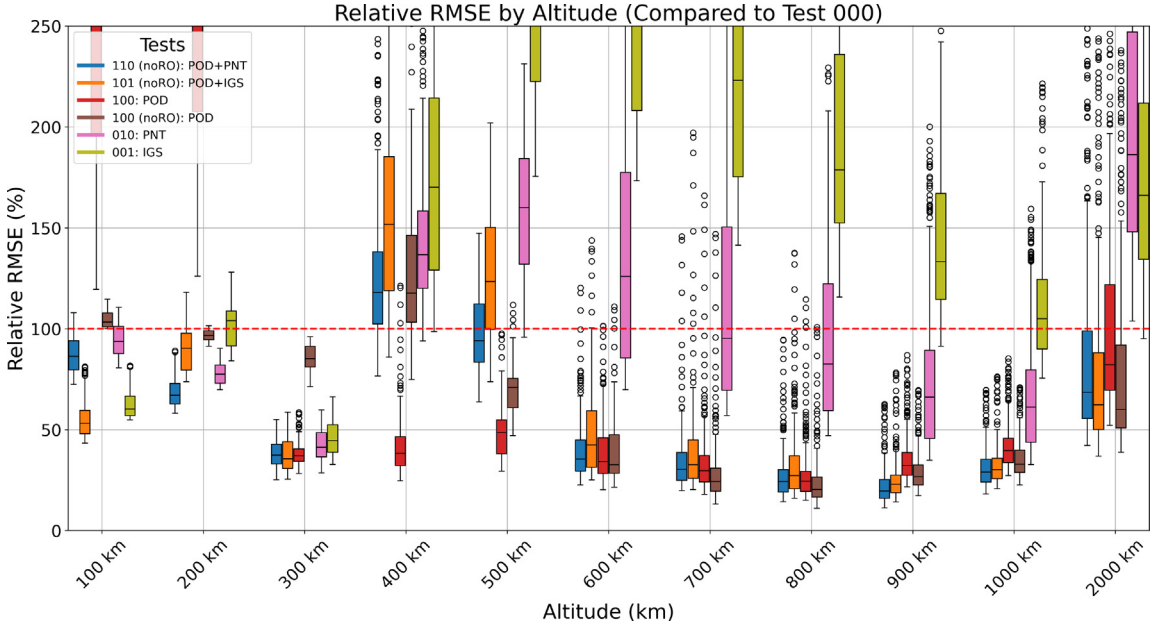

Fig. 15. Same as Fig. 5, but for the remaining cases.

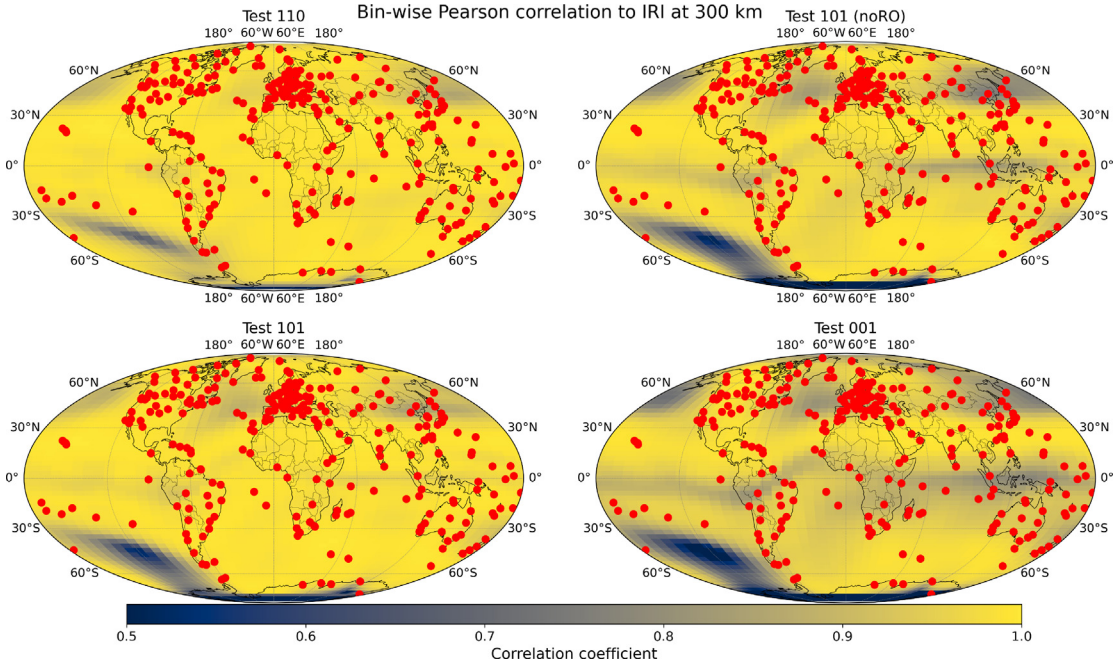

Fig. 16. Extension Fig. 6: Regionally binned correlation between IRI values and the model outputs at 300 km altitude. The coordinates of the used ground station are plotted in red. The comparison includes the cases 110 (PNT + POD), 101 (POD + IGS), 101 without radio occultation, and. 001 (IGS only).

Appendix C. Supplementary data

Supplementary data associated with this article can be found, in the online version, athttps://doi.org/10.1016/j.asr.2026.01.078.

References

Bilitza, D., 1991. The use of transition heights for the representation of ion composition. Adv. Space Res., 11(10), 183–186.https://www.sciencedirect.com/science/article/pii/027311779190341G. doi: 10.1016/0273-1177(91)90341-G.

Bilitza, D., Pezzopane, M., Truhlik, V. et al., 2022. The international reference ionosphere model: a review and description of an ionospheric benchmark. Rev. Geophys., 60(4), e2022RG000792. https://agupubs.onlinelibrary.wiley.com/doi/abs/10.1029/2022RG000792. arXiv:https://agupubs.onlinelibrary.wiley.com/doi/pdf/10.1029/2022RG000792. E2022RG000792 2022RG000792.

Brack, A., Männel, B., Wickert, J. et al., 2021. Operational Multi-GNSS Global Ionosphere Maps at GFZ Derived From Uncombined Code and Phase Observations. Radio Sci., 56(10), e2021RS007337. https://agupubs.onlinelibrary.wiley.com/doi/abs/10.1029/2021RS007337. doi:10.1029/2021RS007337. arXiv:https://agupubs.onlinelibrary.wiley.com/doi/pdf/10.1029/2021RS007337. E2021RS007337 2021RS007337.

Bust, G.S., Mitchell, C.N., 2008. History, current state, and future directions of ionospheric imaging. Rev. Geophys., 46(1). https://agupubs.onlinelibrary.wiley.com/doi/abs/10.1029/2006RG000212. doi: 10.1029/2006RG000212. arXiv:https://agupubs.onlinelibrary.wiley.com/doi/pdf/10.1029/2006RG000212.

ESA, 2025. leo-pnt. esa.int,https://www.esa.int/Applications/Satellite_navigation/LEO-PNT.

Fritsche, M., Dietrich, R., Knöfel, C., et al., 2005. Impact of higher-order ionospheric terms on GPS estimates. Geophys. Res. Lett. 32 (23). https://doi.org/10.1029/2005GL024342, URL: https://agupubs.onlinelibrary.wiley.com/doi/abs/10.1029/2005GL024342. arXiv:https://agupubs.onlinelibrary.wiley.com/doi/pdf/10.1029/2005GL024342.

Gerzen, T., Minkwitz, D., 2016. Simultaneous multiplicative column-normalized method (SMART) for 3-D ionosphere tomography in comparison to other algebraic methods. Ann. Geophys. 34 (1), 97–115. https://doi.org/10.5194/angeo-34-97-2016, URL: https://angeo.copernicus.org/articles/34/97/2016/.

Gurtner, W., Estey, L., 2007. RINEX, The Receiver Independent Exchange Format, Version 3.00. IGS Data Format description, URL: ftp://igs.org/pub/data/format/rinex300.pdf.

Heise, S., Jakowski, N., Wehrenpfennig, A. et al., 2002. Sounding of the topside ionosphere/plasmasphere based on GPS measurements from CHAMP: Initial results. Geophysical Research Letters, 29(14), 44–1–44–4. URL: https://agupubs.onlinelibrary.wiley.com/doi/abs/10.1029/2002GL014738. doi: 10.1029/2002GL014738. arXiv:https://agupubs.onlinelibrary.wiley.com/doi/pdf/10.1029/2002GL014738.

Hoque, M.M., Jakowski, N., 2008. Estimate of higher order ionospheric errors in GNSS positioning. Radio Sci. 43 (5). https://doi.org/10.1029/2007RS003817, URL: https://agupubs.onlinelibrary.wiley.com/doi/abs/10.1029/2007RS003817. arXiv:https://agupubs.onlinelibrary.wiley.com/doi/pdf/10.1029/2007RS003817.

Kelley, M.C., 1989a. Chapter 2 - Fundamentals of Ionospheric Plasma Dynamics. In M.C. Kelley (Ed.), The Earth's Ionosphere (pp. 23–63). Academic Press. URL: http://www.sciencedirect.com/science/article/pii/B9780124040137500071. doi:10.1016/B978-0-12-404013-7.50007-1.

Kelley, M.C., 1989b. The Earth's Ionosphere. Academic Press. https://doi.org/10.1016/B978-0-12-404013-7.X5001-1.

Khodabandeh, A., Teunissen, P.J.G., 2016. Array-aided multifrequency gnss ionospheric sensing: Estimability and precision analysis. IEEE Trans. Geosci. Remote Sens. 54 (10), 5895–5913. https://doi.org/10.1109/TGRS.2016.2574809.

Klobuchar, J.A., 1987. Ionospheric time-delay algorithm for single-frequency gps users. IEEE Trans. Aerosp. Electron. Syst. AES-23(3), 325–331. https://doi.org/10.1109/TAES.1987.310829.

Lomidze, L., Knudsen, D.J., Burchill, J., et al., 2018. Calibration and validation of swarm plasma densities and electron temperatures using ground-based radars and satellite radio occultation measurements. Radio Sci. 53 (1), 15–36. https://doi.org/10.1002/2017RS006415, URL: https://agupubs.onlinelibrary.wiley.com/doi/abs/10.1002/2017RS006415. arXiv:https://agupubs.onlinelibrary.wiley.com/doi/pdf/10.1002/2017RS006415.

Nikoukar, R., Bust, G., Murr, D., 2015a. A novel data assimilation technique for the plasmasphere. J. Geophys. Res.: Space Phys., 120 (10), 8470–8485. URL: https://agupubs.onlinelibrary.wiley.com/doi/abs/10.1002/2015JA021455. doi: 10.1002/2015JA021455. arXiv:https://agupubs.onlinelibrary.wiley.com/doi/pdf/10.1002/2015JA021455.

Nikoukar, R., Bust, G., Murr, D., 2015b. A novel data assimilation technique for the plasmasphere. J. Geophys. Res.: Space Phys., 120 (10), 8470–8485. URL: https://agupubs.onlinelibrary.wiley.com/doi/abs/10.1002/2015JA021455. doi: 10.1002/2015JA021455. arXiv:https://agupubs.onlinelibrary.wiley.com/doi/pdf/10.1002/2015JA021455.

Norberg, J., Virtanen, I.I., Roininen, L., et al., 2016. Bayesian statistical ionospheric tomography improved by incorporating ionosonde measurements. Atmos. Meas. Tech. 9 (4), 1859–1869. https://doi.org/10.5194/amt-9-1859-2016, URL: https://amt.copernicus.org/articles/9/1859/2016/.

Pakhotin, I.P., Burchill, J.K., Förster, M., et al., 2022. The Swarm Langmuir probe ion drift, density and effective mass (SLIDEM) product. Earth, Planets and Space 74 (1), 109. https://doi.org/10.1186/s40623-022-01668-5.

Prol, F., Smirnov, A., Hoque, M., et al., 2022. Combined model of topside ionosphere and plasmasphere derived from radio-occultation and van allen probes data. Scient. Rep. 12, 9732. https://doi.org/10.1038/s41598-022-13302-1.

Prol, F., Smirnov, A., Kaasalainen, S., et al., 2023. The Potential of LEO-PNT mega-constellations for ionospheric 3d imaging: a simulation study. In: IEEE Journal of Selected Topics in Applied Earth Observations and Remote Sensing, pp. 1–13. https://doi.org/10.1109/JSTARS.2023.3299415.

Rich, F., 1994. Users guide for the topside ionospheric plasma monitor (SSIES, SSIES-2 and SSIES-3) on spacecraft of the Defense Meteorological Satellite Program (DMSP). Volume I: Technical Description; PL-TR-94-2187. URL: https://satdat.ngdc.noaa.gov/dmsp/docs/Rich%20-%201994%20-%20Users%20Guide%20SSIES-1%20SSIES-2%20SSIES-3%20-%20PL-TR-94-2187.pdf.

Schaer, S., Beutler, G., Rothacher, M. et al., 1996. Daily Global Ionosphere Maps based an GPS carrier phase data routinely produced by the CODE analysis center. IGS AC Workshop.

Schreiter, L., Brack, A., Männel, B. et al., 2024. Imaging of the ionosphere and plasmasphere using gnss slant tec obtained from leo satellites. Radio Science, 59(12), e2024RS008058. URL: https://agupubs.onlinelibrary.wiley.com/doi/abs/10.1029/2024RS008058. doi: 10.1029/2024RS008058. arXiv:https://agupubs.onlinelibrary.wiley.com/doi/pdf/10.1029/2024RS008058. E2024RS008058 2024RS008058.

Schreiter, L., Stolle, C., Rauberg, J. et al., 2023. Topside Ionosphere Sounding From the CHAMP, GRACE, and GRACE-FO Missions. Radio Sci., 58(3), e2022RS007552. URL: https://agupubs.onlinelibrary.wiley.com/doi/abs/10.1029/2022RS007552. doi:10.1029/2022RS007552. arXiv:https://agupubs.onlinelibrary.wiley.com/doi/pdf/10.1029/2022RS007552. E2022RS007552 2022RS007552.

Schunk, R.W., Scherliess, L., Sojka, J.J. et al., 2004. Global Assimilation of Ionospheric Measurements (GAIM). Radio Sci., 39(1). https://agupubs.onlinelibrary.wiley.com/doi/abs/10.1029/2002RS002794. doi: 10.1029/2002RS002794. arXiv:https://agupubs.onlinelibrary.wiley.com/doi/pdf/10.1029/2002RS002794.

Selmke, I., Dach, R., Arnold, D. et al., 2020. CODE repro3 product series for the IGS. URL: https://www.aiub.unibe.ch/download/REPRO_2020. doi:10.7892/boris.135946.

Simon, D., 2006. Nonlinear kalman filtering. Optimal State Estimation chapter, 13. John Wiley & Sons, Ltd, pp. 393–431. https://doi.org/10.1002/0470045345.ch13, URL: https://onlinelibrary.wiley.com/doi/abs/10.1002/0470045345.ch13. arXiv:https://onlinelibrary.wiley.com/doi/pdf/10.1002/0470045345.ch13.

Smirnov, A., Shprits, Y., Prol, F., et al., 2023. A novel neural network model of Earth's topside ionosphere. Scient. Rep. 13 (1), 1303. https://doi.org/10.1038/s41598-023-28034-z.

Stolle, C., Lilensten, J., Schlüter, S., et al., 2006. Observing the north polar ionosphere on 30 October 2003 by GPS imaging and IS radars. Ann. Geophys. 24 (1), 107–113. https://doi.org/10.5194/angeo-24-107-2006, URL: https://angeo.copernicus.org/articles/24/107/2006/.

Thrun, S., Burgard, W., Fox, D., 2005. Probabilistic Robotics. MIT Press, Cambridge, MA.

Vaishnav, R., Jin, Y., Mostafa, M.G. et al., 2021. Study of the upper transition height using isr observations and iri predictions over arecibo. Advances in Space Research, 68(5), 2177–2185. URL: https://www.sciencedirect.com/science/article/pii/S0273117720307213. doi: 10.1016/j.asr.2020.10.010. International Reference Ionosphere - Progress and New Inputs.

Zhelavskaya, I.S., Aseev, N.A., Shprits, Y.Y., 2021. A combined neural network- and physics-based approach for modeling plasmasphere dynamics. J. Geophys. Res.: Space Phys., 126(3), e2020JA028077. URL: https://agupubs.onlinelibrary.wiley.com/doi/abs/10.1029/2020JA028077. doi: 10.1029/2020JA028077. arXiv:https://agupubs.onlinelibrary.wiley.com/doi/pdf/10.1029/2020JA028077. E2020JA028077 2020JA028077.

Zhelavskaya, I.S., Shprits, Y.Y., Spasojevic, M., 2017. Empirical modeling of the plasmasphere dynamics using neural networks. J. Geophys. Res.: Space Phys., 122(11), 11227–11244. URL: https://agupubs.onlinelibrary.wiley.com/doi/abs/10.1002/2017JA024406. doi: 10.1002/2017JA024406. arXiv:https://agupubs.onlinelibrary.wiley.com/doi/pdf/10.1002/2017JA024406.